The 4SAILT Model: An Improved 4SAIL Canopy Radiative Transfer Model for Sloping Terrain

Hanyu Shi, *Student Member, IEEE*, and Zhiqiang Xiao, *Member, IEEE*

Abstract— The scattering by arbitrary inclined leaves (SAIL)-series models are some of the most well-known and widely used canopy radiative transfer models in the remote-sensing community. The latest version of 4SAIL simulates directional radiance from the optical to thermal spectrum range, but it is not suitable for sloping terrain. This limits its use in the currently ever-expanding development of applications for high-spatial-resolution observations. This study extends the 4SAIL model to 4SAILT, which considers the topographical effects on direct solar radiation and the obstruction of the surrounding topography for hemispherical radiation and the gravitropic influences on leaf angle distribution (LAD). The proposed 4SAILT model was evaluated by the 3-D discrete anisotropic radiative transfer (DART) ray-tracing model for various sky radiation conditions, soil and leaf temperatures, observational geometries, leaf area index values, and six typical LAD functions. The simulated results of directional radiance demonstrated that 4SAILT was consistent with DART, having RMSE values less than 2.0 and 0.1 $W/m^2/\mu m/sr$ over the 0.35–2.5 and 2.5–15 μm spectra, respectively. As an accurate, efficient, and ready-to-use model, 4SAILT benefits those who intend to use SAIL for modeling terrain areas. The 4SAILT model simulates canopy directional radiance, reflectance, emissivity, and brightness temperature over terrain surfaces, through the optical to thermal ranges. It can also be used as a surface model when estimating shortwave, longwave, and net radiation.

Index Terms— 4SAIL, canopy radiative transfer (RT), gravitropism, topography.

I. INTRODUCTION

THE surface energy budget is one of the most important topics in earth system studies, and surface reflective and emissive properties have crucial influences on it [1]. Early earth system models usually assigned particular albedo and emissivity values to specific land types, however, which may have caused significant errors. These particular values have gradually been replaced by the development of remote-sensing techniques and global parameter products [2]–[4]. Modeling the reflective and emissive properties of the terrestrial system is challenging due to its heterogeneity, especially over vegetated areas. Vegetation plays an essential role in the earth's

surface energy balance [5], but the complex structures of plants have made it difficult to accurately model the interactions between canopy and radiation. Even so, many canopy reflectance and emissivity models have been developed, as reviewed in detail by Kuusk [6] and Cao *et al.* [7]. Of those models, the scattering by arbitrary inclined leaves (SAIL) model is widely used in the remote-sensing community for its accuracy and efficiency. The SAIL model [8], [9] is a 1-D canopy radiative transfer (RT) model that extended the Suit model [10], and the hot-spot effect was incorporated in [11] based on the theory proposed in [12]. Then, it was coupled with the leaf optical model PROSPECT to form the PROSAIL (PROSPECT+SAIL) model [13]. Thermal emission by leaves and soil was further modeled and incorporated in SAIL to build the 4SAIL model [14]. Therefore, the 4SAIL model simulates the canopy RT process throughout the optical to thermal ranges.

The PROSAIL model has been used in the production of the Carbon cYcle and Change in Land Observational Products from an Ensemble of Satellites (CYCLOPES) global leaf area index (LAI) and the fraction of absorbed photosynthesis active radiation (FAPAR) products, which have moderate spatial resolutions of 300–1000 m. Similar moderate-spatial-resolution parameter products include the Advanced Very High Resolution Radiometer (AVHRR) and Moderate Resolution Imaging Spectroradiometer (MODIS) products. These products have achieved significant success in land-cover and land-use change, climate change, carbon cycles, and vegetation phenology.

In recent years, the development of applications using high-spatial-resolution data has grown, and observations (e.g., from Landsat and Sentinel satellites) are capable of satisfying the demands for data. However, the topographic effect is an inevitable factor when processing high-spatial-resolution data since it changes solar-target-sensor geometries, affects radiation fields, and alters the radiance observed by sensors [15]. Many studies have demonstrated that neglecting topographic effects induces uncertainties in parameter estimation [15]–[32]. For example, Lipton and Ward [17] found errors larger than 9 K in land surface temperature estimation if terrain features are neglected. Gemmell *et al.* [18] found that neglecting topographic effects induced a significant error in estimating forest coverage. Gonsamo and Chen [25] found clear differences in the estimated LAI over mountainous areas when using the algorithms with and without taking topography into account. Mousivand *et al.* [15] found that the error

in the retrieved LAI larger than 0.5 if topographic effects were ignored. In addition, the importance of topographic effects on the estimation of shortwave [19], [20], [23] and longwave [27], [30], [31] surface radiation has been reported in many studies. Some models have been developed that account for topographic effects, including surface reflectance models (for the shortwave range) and surface emissivity or brightness temperature models (for the thermal range).

In the shortwave range, most of the topographic models are extensions of existing flat-surface models, roughly divided into three categories: the geometric optical (GO) models [33], [34], the RT models [35], [36], and hybrid of GO–RT models [37]–[40]. RT-based models handle diffuse solar radiation and multiple scattering processes well. Yin *et al.* [36] adopted a similar framework with the SAIL model to simulate canopy reflectance over slopes. A path-length-correction (PLC)-based model was proposed in Yin *et al.*, and it adopted the PLC method to calculate the single-order scattering. However, the topographic effects on diffuse scattering are only approximately modeled by the PLC model. Combal *et al.* [35] extended the turbid canopy modeling approach for sloping terrains, which was a far-sighted work. Unfortunately, they built the theory from RT equations and assumed black soil to focus on the effects of canopies, which means that it is not a ready-to-use model. Both the GO and hybrid models have mainly been developed for forest canopies with specific crown shapes, and they generally perform well for discontinuous canopies. However, GO theory-based models usually assume Lambertian component reflectances, and the contributions of diffuse solar radiation and multiple scattering among the different components are usually not well modeled [40]. Thus, RT modeling approaches are often incorporated. The GOST-series models [37]–[39] introduced photon recollision probability theory to account for multiple scattering. Wu *et al.* [40] tried to combine the GO and the RT approaches to account for the anisotropic reflectance of crowns by using the SAIL model to simulate crown reflectance and transmittance. There are fewer emissivity models with topographic effects for thermal applications than reflectance models in the shortwave range. Most studies have been from the perspective of modeling longwave irradiance with topographic effects [27], [41]–[45] and/or built with the scaling of temperature or radiance at different scales with the consideration of subpixel topography [16], [17], [26], [31], [46], in which the subpixels were assumed to have isotropic emissivity or in which the cosine correction methods were applied [47].

All the terrain models summarized earlier have their own characteristics and suit different applications; however, they model the optical and thermal features separately. Unified optical–thermal RT models are not very common at present, but the 4SAIL model is one such model: 4SAIL is a unified optical–thermal canopy RT model for flat surfaces and has been proven to be efficient and accurate [14], but it is not designed for terrain surfaces. Of course, 3-D ray-tracing-, radiosity-, and Monte-Carlo-based models simulate topographic effects well by building terrain scenes and often cover both the shortwave and longwave ranges [48]–[53]. However, such 3-D models are computationally expensive and

time-consuming. Thus, they are often used as benchmarks for evaluations, rather than for estimating parameters.

In this study, the well-known 4SAIL model was extended for terrain surfaces to develop 4SAILT (4SAIL for Terrain surfaces) model, which was evaluated by the 3-D discrete anisotropic radiative transfer (DART) ray-tracing model [49]–[51]. The 4SAIL model was selected because it has been widely used, and it is one of the few 1-D optical–thermal models. The combined effects of topography and gravitropism were modeled and analyzed. Modeling the combined effects of topography and gravitropism is described in Section II and further evaluated and analyzed in Section III. A brief discussion and conclusion is given in Section IV.

II. METHODOLOGY

The calculation of directional radiance in 4SAIL is first given before proposing the 4SAILT model. In the 4SAIL model, the flux-equivalent radiance in the view direction (E_o) is given [8], [14] as

$$
E_o = r_{so}^* E_{dir} + r_{do}^* E_{dif} + \varepsilon_v^* H_c + \varepsilon_s^* H_d \\
+ \varepsilon_v^{**} (H_h - H_c) + \varepsilon_s^{**} (H_s - H_d) \quad (1)
$$

where E_{dir} and E_{dif} are the incident direct and diffuse irradiance, respectively; E_{dif} is the sum of the downward diffuse solar irradiance (E_d) and downward atmospheric thermal irradiance (E_a), i.e., $E_{dif} = E_d + E_a$. $H_h, H_c, H_s,$ and H_d are the hemispherical thermal fluxes associated with the blackbody hot leaves, cold leaves, hot soil, and cold soil, respectively, and $H = \pi B(T)$, where B is Planck's radiance function and T is the temperature.

The step-by-step derivation of the 4SAIL model and the definitions and calculations of $r_{so}^*, r_{do}^*, \varepsilon_v^*, \varepsilon_s^*, \varepsilon_v^{**},$ and ε_s^{**} are given in Appendix A.

A. 4SAILT Model

1) Topographic Algorithm: Before building the 4SAILT model, the coordinates used for modeling and a general topographic algorithm from [15] and [54] is first defined and introduced. As shown in Fig. 1, the XYZ coordinate system is built for the flat surface, whereas the PQR coordinate is for surfaces with a slope of β and an aspect of φ. Thus, the normal to the flat surface is $\boldsymbol{n}$, and the normal to the slope is $\boldsymbol{t} = (\sin\beta\cos\varphi; \sin\beta\sin\varphi; \cos\beta)$ in the XYZ coordinate. The reflection properties of a surface are characterized by $r_{so}, r_{sd}, r_{do},$ and r_{dd} (see Table II in Appendix A for the physical explanations), and the temperature of the surface is T. The bottom of atmosphere (BOA) irradiance is composed of direct irradiance E_{dir} and isotopic diffuse irradiance E_{dif}.

A direction can be expressed using a vector $\boldsymbol{p}^h = \left(\sin\theta_p^h\cos\varphi_p^h; \sin\theta_p^h\sin\varphi_p^h; \cos\theta_p^h\right)$ in the XYZ coordinates and $\boldsymbol{p}^t = \left(\sin\theta_p^t\cos\varphi_p^t; \sin\theta_p^t\sin\varphi_p^t; \cos\theta_p^t\right)$ in PQR coordinates. θ_p^h and φ_p^h (superscript "h" indicates the XYZ coordinate for flat surfaces) are the zenith and azimuth angles in the XYZ coordinates, respectively; and θ_p^t and φ_p^t (superscript "t" indicates the PQR coordinate for terrain surfaces) are the zenith and azimuth angle in the PQR coordinates, respectively. The transformation between $\boldsymbol{p}^h$ and $\boldsymbol{p}^t$ is

$$
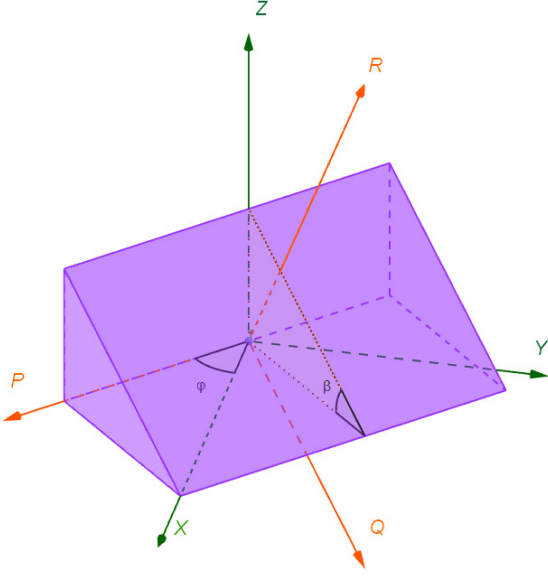\boldsymbol{p}^t = R_y(\beta)R_z(\varphi)\boldsymbol{p}^h \quad (2)
$$

Fig. 1. Coordinates for a horizontal surface (XYZ) and a sloping surface (PQR). The slope and aspect values are β and φ, respectively. For interpretation of the references to color in this figure legend, the reader is referred to the web version of this article.
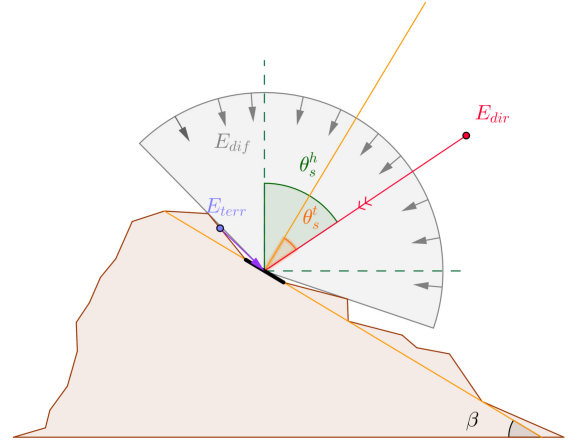

Fig. 2. Topographic effects on the radiation received by a sloping surface (pixel). The red arrow indicates direct solar radiation. The gray arrows indicate diffuse radiation from the sky. The purple arrow indicates the radiation from surrounding surfaces (pixels). The dashed horizontal green line represents a horizontal plane, and the dashed vertical green line represents the normal to the horizontal plane. This figure is adapted from [15, Fig. 3]. For interpretation of the references to color in this figure legend, the reader is referred to the web version of this article.

where R_z and R_y are the rotation matrices

$$
R_z(\varphi) = \begin{bmatrix} \cos\varphi & \sin\varphi & 0 \\ -\sin\varphi & \cos\varphi & 0 \\ 0 & 0 & 1 \end{bmatrix}
$$
$$
R_y(\beta) = \begin{bmatrix} \cos\beta & 0 & -\sin\beta \\ 0 & 1 & 0 \\ \sin\beta & 0 & \cos\beta \end{bmatrix}. \tag{3}
$$

If the surface is horizontally placed (the XY plane or an XY-parallel plane), then the observed radiance L_o is given by

$$
L_o = \frac{1}{\pi} \left[r_{so}\left(\Omega_s^h; \Omega_o^h\right) E_{\mathrm{dir}}\left(\Omega_s^h\right) \right.
$$
$$
\left. + r_{do}\left(\Omega_{2\pi}^h; \Omega_o^h\right) E_{\mathrm{dif}}\left(\Omega_{2\pi}^h\right) + \pi\varepsilon\left(\Omega_o^h\right) B(T) \right] \tag{4}
$$

where $\Omega_s^h(\theta_s^h, \varphi_s^h)$ and $\Omega_o^h(\theta_o^h, \varphi_o^h)$ are the sunlight and view directions, respectively, in XYZ coordinates; as shown in Fig. 2, θ_s^h is the angle between sunray and the normal to the horizontal plane, $\Omega_{2\pi}^h$ indicates the diffuse radiation in hemispherical space, and $E_{\mathrm{dir}}(\Omega_s^h)$ and $E_{\mathrm{dif}}(\Omega_{2\pi}^h)$ are the incident direct and diffuse irradiance, respectively, referred to the horizontal plane.

If the horizontal surface is rotated to the slope shown in Fig. 1 (the PQ or a PQ-parallel plane), L_o is given by

$$
L_o = \frac{1}{\pi} \left[r_{so}\left(\Omega_s^t; \Omega_o^t\right) E_{\mathrm{dir}}\left(\Omega_s^t\right) \right.
$$
$$
+ r_{do}\left(\Omega_{2\pi}^t; \Omega_o^t\right) E_{\mathrm{dif}}\left(\Omega_{2\pi}^t\right) + \pi\varepsilon\left(\Omega_o^t\right) B(T)
$$
$$
\left. + r_{do}\left(\Omega_{2\pi}^t; \Omega_o^t\right) E_{\mathrm{terr}} \right] \tag{5}
$$

where $\Omega_s^t(\theta_s^t, \varphi_s^t)$ and $\Omega_o^t(\theta_o^t, \varphi_o^t)$ are the sunlight and view directions in PQR coordinates, respectively θ_s^t is the angle between the sunray and the normal to the sloping plane, shown in Fig. 2; $E_{\mathrm{dir}}(\Omega_s^t)$ and $E_{\mathrm{dif}}(\Omega_{2\pi}^t)$ are the incident direct and diffuse irradiance, respectively, relative to the sloping plane;

and E_{terr} is the irradiance from the adjacent slopes visible from the current pixel (pixel M) and is accurately calculated [54] by

$$
E_{\mathrm{terr}} = \sum_{i=1}^{N} \frac{\cos T_M \cos T_P dS_P}{r_{MP}^2} L_o^{\mathrm{adj}}(i) \tag{6}
$$

where T_M and T_P are the angles of points M and P between the normal vector of the inclined surface and the line MP, r_{MP} is the distance between M and P, L_o^{adj} is the reflected/emitted radiance of P, and dS_P is the area of pixel P. In practical applications, E_{terr} is ignored in the first iteration since (5) and (6) are mutually dependent. Because it is an iterative process, it can be seen that accurate calculation of E_{terr} is computationally expensive.

E_{terr} is usually relatively insignificant and may be neglected in most cases; however, its contribution is important for highly reflective surfaces or in areas with deep valleys [15], [30], [31], [55]. In this study, E_{terr} was not calculated because its contribution is small for vegetated areas and E_{terr} is essentially model-independent, and its accuracy depends on $[r_{so}(\Omega_s^t; \Omega_o^t) E_{\mathrm{dir}}(\Omega_s^t) + r_{do}(\Omega_{2\pi}^t; \Omega_o^t) E_{\mathrm{dif}}(\Omega_{2\pi}^t) + \pi\varepsilon(\Omega_o^t) B(T)]$, i.e., the first three components of (5): thus, if a model gives accurate results without considering E_{terr}, this model can also be used to calculate L_o with E_{terr} accurately.

The transformation between Ω_s^t and Ω_s^h is achieved using (2). The transformations for BOA irradiance between the horizontal and topographic coordinates [15] are

$$
E_{\mathrm{dir}}\left(\Omega_s^t\right) = F_{\mathrm{sun}} E_{\mathrm{dir}}\left(\Omega_s^h\right) \tag{7a}
$$
$$
E_{\mathrm{dif}}\left(\Omega_{2\pi}^t\right) = F_{\mathrm{sky}} E_{\mathrm{dif}}\left(\Omega_{2\pi}^h\right) \tag{7b}
$$
$$
F_{\mathrm{sun}} = \zeta \frac{(\boldsymbol{p}^t \cdot \boldsymbol{n})}{(\boldsymbol{p}^h \cdot \boldsymbol{n})} = \zeta \frac{\cos\theta_s^t}{\cos\theta_s^h} \tag{7c}
$$
$$
F_{\mathrm{sky}} = k \frac{\cos\theta_s^t}{\cos\theta_s^h} + (1-k) V_{\mathrm{sky}} \tag{7d}
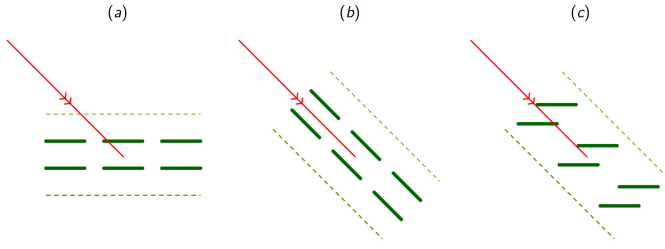$$

Fig. 3. Illustration of the combined influences of topography and gravitropism on leaves. Red lines with arrows are sun rays. Green solid lines represent leaves. (a) Interaction of sunlight with leaves over a flat surface (assume that leaves are parallel to the horizontal plane [i.e., $\theta_l = 0$]). Interaction of sunlight with leaves over a sloping surface: (b) Without considering gravitropism. (c) With gravitropism considered. For interpretation of the references to color in this figure legend, the reader is referred to the web version of this article.

where F_{sun} and F_{sky} are the transformation factors for direct and diffuse radiation, respectively; ζ is a binary factor (0 or 1) that indicates whether the pixel is self-shadowed or shielded by other pixels [15], [56], [57]; F_{sky} considers both the isotropic and anisotropic circumsolar diffuse irradiance; and k is the ratio of isotropic and anisotropic components [15], [58]. In practice, k can be replaced by the direct transmittance of the atmosphere [15], [58]; however, in this study, the isotropic diffuse radiation assumption was adopted. Thus, $F_{\text{sky}} = V_{\text{sky}}$, where V_{sky} is the sky view factor, defined as the relative proportion of the solid angle of the sky. Many different methods have been developed to calculate V_{sky} and the intercomparison among these methods is also conducted [57], [59]–[62].

Therefore, the observed radiance may easily be solved using (2)–(7) since $E_{\text{dir}}(\Omega_s^h)$, $E_{\text{dif}}(\Omega_{2\pi}^h)$, Ω_s^h, Ω_o^h, β, and φ are known.

2) Model Implementation: It is very convenient to apply the topographic algorithm proposed in Section II-A1 for surfaces covered by soil, rock, or snow. However, more detail is involved when using the algorithm for a vegetation canopy because of the gravitropism of plants. Because the leaves cannot simply be rotated, the leaf angle distribution (LAD) must be remodeled. The LAD determines the extent to which radiation interacts within the canopy layer. Its importance on canopy directional radiance has been demonstrated in many studies [63]. An illustration is given in Fig. 3. Assuming that the leaves are parallel to the horizontal plane (i.e., planophile LAD), the interaction of sunlight with the leaves over a flat surface is shown in Fig. 3(a). After rotating the canopy layer, the sunlight-leaf interactions without and with considering gravitropism are shown in Fig. 3(b) and (c), respectively. There is no doubt that the modeling scheme in Fig. 3(b) would induce more significant errors than the arrangement in Fig. 3(c). This simple schematic clearly demonstrates the importance of incorporating gravitropism in terrain canopy models.

The transformation between the XYZ and the PQR coordinate systems for leaves must be applied to model the gravitropism influences. Assume that a leaf has zenith angle θ_l^h and azimuth angle φ_l^h in the XYZ coordinates; then, the zenith angle θ_l^t and the azimuth angle φ_l^t in the PQR coordinates are calculated from

$$l^t = R_y(\beta)R_z(\varphi)l^h \qquad (8)$$

where $l^h = \left(\sin\theta_l^h \cos\varphi_l^h; \ \sin\theta_l^h \sin\varphi_l^h; \ \cos\theta_l^h\right)$ and $l^t = \left(\sin\theta_l^t \cos\varphi_l^t; \ \sin\theta_l^t \sin\varphi_l^t; \ \cos\theta_l^t\right)$.

As described in Appendix A, the assumption of leaf-azimuth independence is used in 4SAIL, and (18) is used to calculate the nine SAIL coefficients in (13). However, the effect of gravitropism invalidates this assumption when taking the PQR coordinates as the reference system. Therefore, the SAIL coefficient (c) is calculated (i.e., (18) is replaced) by

$$c = \int_0^{2\pi} \int_0^{\pi/2} c\left(\theta_l^t, \varphi_l^t\right) g\left(\theta_l^t, \varphi_l^t\right) \sin\theta_l^t \, d\theta_l^t \, d\varphi_l^t \qquad (9)$$

where $g(\theta_l^t, \varphi_l^t)$ is the leaf area orientation density function (some references use $(1/2\pi)g(\theta_l^t, \varphi_l^t)$, but the terminology in [8] and [11] retained here to be consistent). If LAD is independent of the azimuth angle (such as in the 4SAIL model for flat surfaces), $g(\theta_l^h, \varphi_l^h)$ can be replaced by the leaf inclination density function (LIDF) $f(\theta_l^h)$

$$f\left(\theta_l^h\right) = 2\pi g\left(\theta_l^h, \varphi_l^h\right) \sin\theta_l^h. \qquad (10)$$

However, (10) does not work for terrain surfaces and

$$f\left(\theta_l^t\right) = \int_0^{2\pi} g\left(\theta_l^t, \varphi_l^t\right) \sin\theta_l^t \, d\varphi_l^t \neq 2\pi g\left(\theta_l^t, \varphi_l^t\right) \sin\theta_l^t. \qquad (11)$$

Therefore, the SAIL coefficients are calculated from (10) and (18) in 4SAIL, whereas in 4SAILT, (8) is applied to transform $(\theta_l^h, \varphi_l^h)$ to $(\theta_l^t, \varphi_l^t)$, which is then input to (9) to calculate SAIL coefficients.

Combining (8)–(9) with the topographic algorithm proposed in Section II-A1, the observed radiance over a sloping surface in 4SAILT is given by

$$
\begin{aligned}
L_o = \frac{1}{\pi} \Big[& r_{so}^*\left(\Omega_s^t; \Omega_o^t\right) F_{\text{sun}} E_s\left(\Omega_s^h\right) \\
+ \ & r_{do}^*\left(\Omega_{2\pi}^t; \Omega_o^t\right) F_{\text{sky}} E_d\left(\Omega_{2\pi}^h\right) \\
+ \ & r_{do}^*\left(\Omega_{2\pi}^t; \Omega_o^t\right) F_{\text{sky}} E_a\left(\Omega_{2\pi}^h\right) \\
+ \ & \varepsilon_v^*\left(\Omega_o^t\right) H_v + \varepsilon_s^*\left(\Omega_o^t\right) H_s \\
+ \ & \varepsilon_v^{**}\left(\Omega_o^t\right)(H_h - H_c) + \varepsilon_s^{**}\left(\Omega_o^t\right)(H_s - H_d) \Big]
\end{aligned} \qquad (12)
$$

where $E_s(\Omega_s^h)$, $E_d(\Omega_s^h)$, and $E_a(\Omega_s^h)$ are the downward direct solar irradiance, downward diffuse solar irradiance, and downward atmospheric thermal irradiance on the horizontal plane, respectively.

B. Evaluation Scheme

The proposed 4SAILT model was evaluated by the well-known 3-D DART model, which is often used as a benchmark [49]–[51]. The DART model discretizes the Earth scene into many voxels and simulates any scene, depending to the applications. Both the DART and 4SAIL/4SAILT models require leaf and soil spectra as input. Although the PROSPECT model [64] is often used to simulate leaf spectra, it only covers a range from 400 to 2500 nm. Instead, without loss of generality, the leaf and soil spectra (0.35–15 μm) were inputted in this study [see Fig. 4(a)].

The BOA irradiance was presimulated according to atmospheric conditions and solar positions using the MODerate resolution atmospheric TRANsmission (MODTRAN)
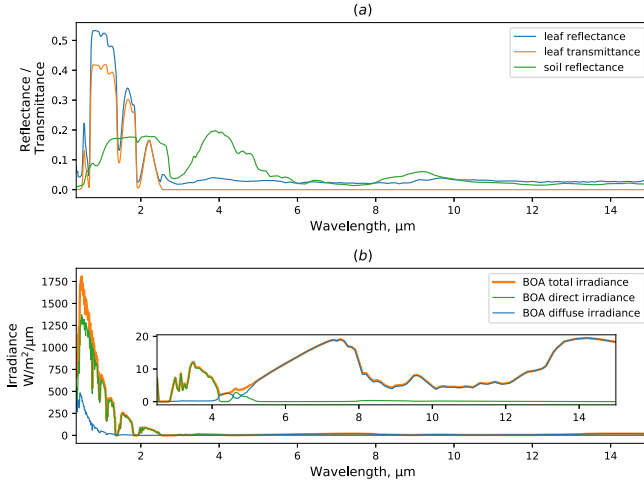
Fig. 4. (a) Leaf and soil spectra used in this study. (b) Example of BOA irradiance (in $W/m^2/\mu m$) spectra used in this study, which corresponds to an aerosol atmosphere with the AOD of 0.2. The solar zenith angle is 15°. The subplot in (b) is for the irradiance from 2.5 to 15 μm. For interpretation of the references to color in this figure legend, the reader is referred to the web version of this article.

TABLE I
PARAMETER SETTINGS FOR COMPARING DART AND 4SAILT MODELS. LAD = LEAF ANGLE DISTRIBUTION

Parameter	Values	Units
For MODTRAN	molecular atmosphere aerosol atmosphere cloud atmosphere	-
Solar zenith angle	5, 15, 25, 35	degrees
Solar azimuth angle	0	degrees
View zenith angle	0, 10, 20, 30, 40	degrees
View azimuth angle	0, 90, 180, 270	degrees
Slope	10, 40	degrees
Aspect	0, 90, 180	degrees
Leaf area index	1, 3, 6	m^2/m^2
LAD	uniform, spheric, erectophile, planophile, extremophile, plagiophile	-
Leaf temperature	10, 30	°C
Soil temperature	10, 30	°C

model and is input into the DART and 4SAILT models to simulate sensor radiance. The parameter settings for model comparison are shown in Table I. Three atmospheric conditions are predefined: a molecular atmosphere, an aerosol atmosphere with an aerosol optical depth (AOD) of 0.2, and a cloudy atmosphere with a cloud optical depth of 8.0. The 1976 U.S. standard atmosphere, the rural aerosol type, and the default standard cirrus model are used. One BOA irradiance spectrum is shown in Fig. 4(b), in which the direct and diffuse incident radiation is also plotted. For terrain conditions, a gentle slope (10°) and a steep slope (40°) were configured. The solar and view zenith angles relative to the horizontal plane ranged from 0° to 40°; thus, the corresponding zenith angle relative to the slope spans from 0° to 80°. Three LAI values and six typical
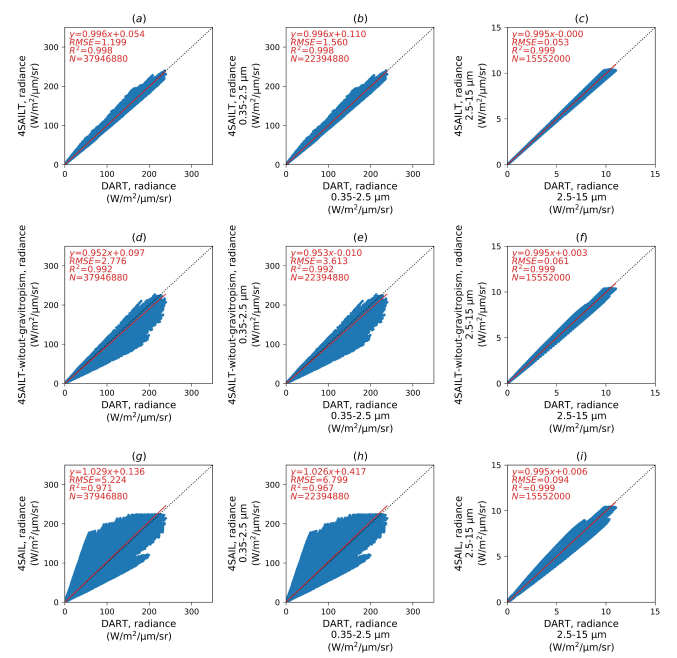

Fig. 5. Evaluation of the radiance (in $W/m^2/\mu m/sr$) simulated by (a)–(c) proposed 4SAILT model, (d)–(f) 4SAILT-without-gravitropism, and (g)–(i) 4SAIL models. Scattergrams for 0.35–15.0, 0.35–2.5, and 2.5–15.0 μm are plotted separately. For interpretation of the references to color in this figure legend, the reader is referred to the web version of this article.

LAD functions were simulated. Both the leaf and soil were treated as isothermal objects (i.e., no temperature differences within leaves and within soil). The simulations were conducted at a 10-nm interval between 0.35 and 2.5 μm, a 50-nm interval for 2.5–5.5 μm, and a 100-nm interval for 5.5–15.0 μm. For convenience, the approximation method proposed in [59] was used in this study to calculate V_{sky}. In practical applications, more accurate methods may be adopted, with the help of the digital elevation model (DEM) data [56], [57], [62].

III. RESULTS AND ANALYSES

A. Model Evaluation

The proposed 4SAILT model was evaluated by comparing with DART, and the results from the 4SAIL model and the 4SAILT-without-gravitropism (4SAILT model without considering gravitropism effects) model were also compared.

Fig. 5 shows the scatter plots for the modeled radiance and the DART radiance. The comparative results between 4SAILT and DART are given in the first row of Fig. 5 (a)–(c). The overall scatter plot is shown in Fig. 5(a); the optical part and the infrared-thermal part are shown in Fig. 5(b) and (c). It is seen that the 4SAILT model generally agreed well with the DART model, with an overall RMSE value less than 1.2 $W/m^2/\mu m/sr$ and $R^2 > 0.99$. The second row of Fig. 5 compares the 4SAILT-without-gravitropism and the DART models. It shows that ignoring gravitropic effects introduced errors, especially in the shortwave spectrum range. Fig. 5(g)–(i) compares 4SAIL and DART. Significant differences were observed in the results, which demonstrated that
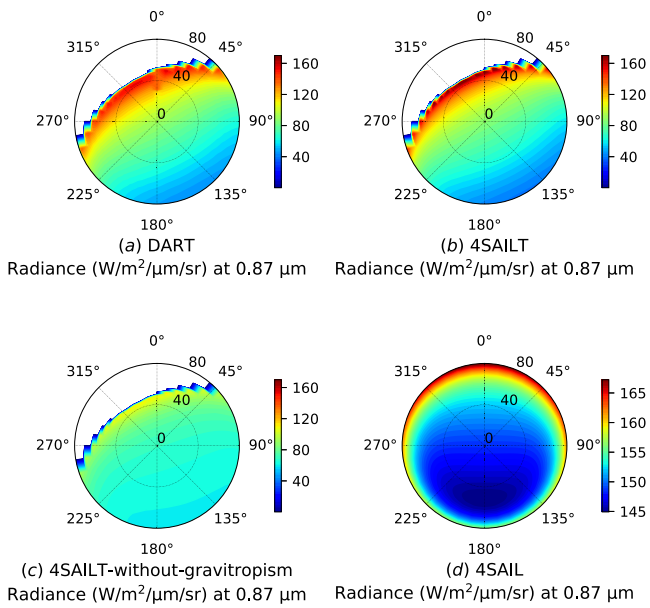
Fig. 6. Comparisons of radiance (W/m²/μm/sr) simulated over 2π space by (a) DART, (b) 4SAILT, (c) 4SAILT-without-gravitropism, and (d) 4SAIL models (0.87 μm simulation—Planophile LAD, solar zenith 25°, azimuth angle 0°, slope 45°, and aspect 150°). For interpretation of the references to color in this figure legend, the reader is referred to the web version of this article. (a) DART radiance (W/m²/μm/sr) at 0.87 μm. (b) 4SAILT radiance (W/m²/μm/sr) at 0.87 μm. (c) 4SAILT-without-gravitropism radiance (W/m²/μm/sr) at 0.87 μm. (d) 4SAIL radiance (W/m²/μm/sr) at 0.87 μm.

Fig. 7. 10.5 μm simulation. Parameters as in Fig. 6. The temperatures of soil and leaf are set as 40 °C and 25 °C, respectively, in the simulation. For interpretation of the references to color in this figure legend, the reader is referred to the web version of this article. (a) DART radiance (W/m²/μm/sr) at 10.5 μm. (b) 4SAILT radiance (W/m²/μm/sr) at 10.5 μm. (c) 4SAILT-without-gravitropism radiance (W/m²/μm/sr) at 10.5 μm. (d) 4SAIL radiance (W/m²/μm/sr) at 10.5 μm.

ignoring topographic effects induced errors within both the optical and the thermal regions.

Examples of the distribution of radiance for hemispherical space are shown in Fig. 6 (simulated at 0.87 μm) and Fig. 7 (simulated at 10.5 μm). The BOA irradiance corresponds to the aerosol atmosphere defined in Table I for a solar zenith angle is 25°. The slope and aspect are 45° and 150°, respectively, and the planophile LAD was used.

The no-data regions in Figs. 6 and 7 indicate that the sensor cannot see the current scene. It is shown that 4SAILT had the same distribution patterns as DART, whereas 4SAIL did not capture the effects of topography. Also, although the basic patterns from the 4SAIL-without-gravitropism model were to some extent similar to those from DART and 4SAILT, they differed in detail (e.g., the bottom-left parts of the subplots in Figs. 6 and 7).

The results at the solar plane are plotted in Fig. 8, which shows that the 4SAILT model was consistent with DART, while others failed to capture the patterns. Fig. 8 shows the importance of the gravitropism effect and neglecting it results in differently shaped curves. The DART simulations showed some fluctuations in the hemispherical and curve plots, the reason being that DART discretized the canopy into many voxels; thus, the boundary of the canopy was not modeled perfectly smoothly over terrain surfaces (this problem does not arise over flat surfaces).

B. Influences of Topography

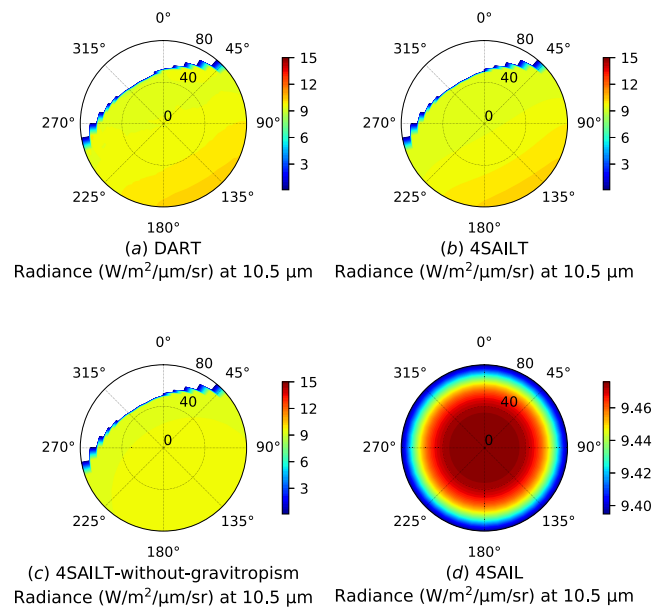The errors induced by ignoring topographic effects were analyzed for different slopes using the 4SAIL and 4SAILT

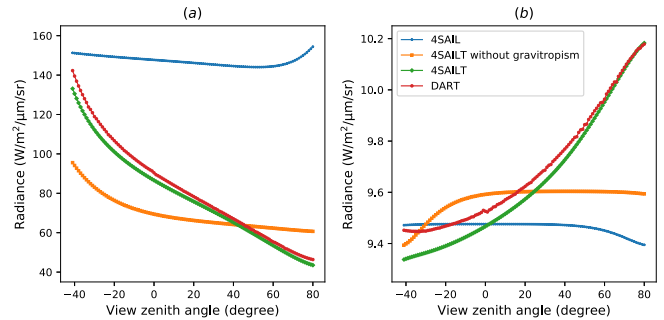Fig. 8. Comparisons of radiance (W/m²/μm/sr) simulated by DART, 4SAILT, 4SAILT-without-gravitropism, and 4SAIL at the solar plane. (a) 0.87 μm. (b) 10.5 μm. For interpretation of the references to color in this figure legend, the reader is referred to the web version of this article.

models. The parameter configurations were expanded from Table I, with slope values from 0° to 60° at 10° intervals.

The percentage differences in the simulated radiance by the 4SAIL and 4SAILT models for increasing terrain slope (calculated as (4SAIL–4SAILT)/4SAILT × 100%) are shown as boxplots in Fig. 9. The figure shows that the difference in radiance increases with slope angle and exceeds 60% for a 60° slope. The absolute differences of radiance between 4SAIL and 4SAILT in the range 0.35–15 μm are shown in Fig. 10, in which Fig. 10(a) and (b) shows the averaged and the maximum differences, respectively. The averaged differences of radiance increased with slope span the spectrum 0–50 W/m²/μm/sr. The maximum differences exceeded 200 W/m²/μm/sr if the topographic effects were not considered. Figs. 9 and 10 show that ignoring topographic effects introduces significant errors.
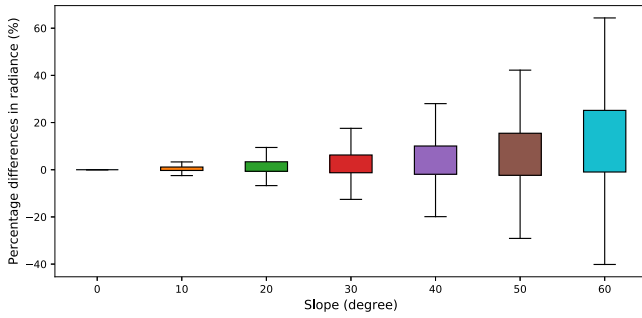
Fig. 9. Percentage differences in radiance (W/m²/μm/sr) simulated by the 4SAIL and 4SAILT models with increasing terrain slope. For interpretation of the references to color in this figure legend, the reader is referred to the web version of this article.
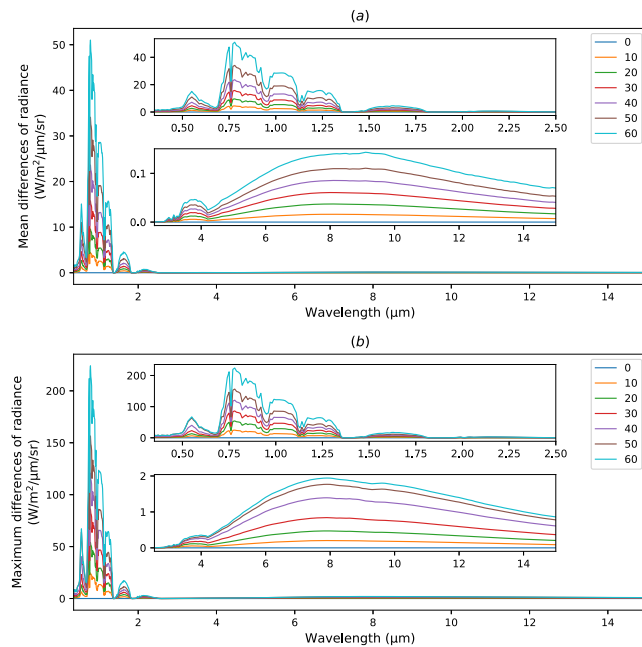

Fig. 10. Absolute differences of radiance (W/m²/μm/sr) simulated by the 4SAIL and 4SAILT models for 0.35–15 μm. (a) Mean differences. (b) Maximum differences. For interpretation of the references to color in this figure legend, the reader is referred to the web version of this article.

IV. CONCLUSION AND DISCUSSION

The 4SAIL model is improved for terrain slopes and forms the 4SAILT model. By adding three terrain variables (i.e., slope, aspect, and F_{sky}), the 4SAILT model simulates observed radiance over sloping surfaces in the optical-to-thermal spectra. Other parameters, such as reflectance, emissivity, and brightness temperature, can also be simulated. However, because these are all derived from radiance, they are not separately discussed in this study. The 4SAILT can also be used as the surface model when estimating shortwave, longwave, and net radiation.

Evaluation of the 4SAILT model by comparison with the 3-D DART model showed that it was consistent with DART. The 4SAILT model considers topographic and gravitropic influences. The evaluation results showed that ignoring them

induced errors up to 200 W/m²/μm/sr over a series of slope values. As an accurate and efficient model, 4SAILT may be used both for forward modeling and parameter inversion studies. In addition, the topographic and gravitropic algorithm was suitable for not only the SAIL model but also other canopy models.

The lack of validating 4SAILT by field measurements is a shortage of this study. However, various solar, sensor, and terrain conditions can be configured by comparing 4SAILT with DART, and thus, a comprehensive evaluation has been conducted, which is difficult or even impractical to achieve for field measurements. Nevertheless, a field experiment is planned and the comparisons with field data are expected in the future.

Composite slopes [65], i.e., the rugged terrains, were not considered in the current study; however, for moderate-spatial-resolution observations such as MODIS, it is an inevitable topic. Usually, observations (e.g., Landsat), DEM data (e.g., ASTER DEM), and models at the subpixel level are needed. The 4SAILT is an accurate, efficient and ready-to-use model suitable for direct incorporation into methods for composite slopes (see [31], [46], [66], [67]), which provide methods, directly or indirectly, for composite slopes. Besides, by incorporating (6), the proposed 4SAILT also works for composite slopes or complex terrain surfaces, which will be tested in the near future.

APPENDIX

A. 4SAIL Model

In the 4SAIL model for flat surfaces, the four-stream differential equations for direct solar irradiance (E_s), downward diffuse irradiance (E^-), upward diffuse irradiance (E^+), and flux-equivalent radiance in view direction (E_o) are given [8], [14] as

$$\frac{dE_s}{Ldx} = kE_s \tag{13a}$$

$$\frac{dE^-}{Ldx} = -s'E_s + aE^- - \sigma E^+ - \varepsilon_v H_v \tag{13b}$$

$$\frac{dE^+}{Ldx} = sE_s + \sigma E^- - aE^+ + \varepsilon_v H_v \tag{13c}$$

$$\frac{dE_o}{Ldx} = wE_s + vE^- + v'E^+ - KE_o + K\varepsilon_v H_v \tag{13d}$$

where L is the LAI, x is the relative optical height (-1 at the bottom of the canopy and 0 at the top), ε_v is the emissivity of the leaf, and H_v is the hemispherical flux calculated for blackbody leaves at temperature T_v

$$H_v = \pi B(T_v) \tag{14}$$

where B is Planck's radiance function; k and K are the extinction coefficients for direct flux in sunlight and view directions, respectively; w is the bidirectional scattering coefficient of the canopy; s and s' are the back and forward scattering coefficient for direct radiation, respectively; v and v' are scattering coefficients for downward and upward diffuse radiation into view direction, respectively; σ and σ' are the diffuse back and forward scattering coefficient, respectively;

and a is the attenuation coefficient. These extinction and scattering coefficients are functions of θ_l and φ_l, which are the zenith angle and azimuth angle of the leaf's upward normal [8], [11]

$$k(\theta_l, \varphi_l) = |f_s| \tag{15a}$$

$$K(\theta_l, \varphi_l) = |f_o| \tag{15b}$$

$$w(\theta_l, \varphi_l) = f_s \rho f_o \quad \text{or} \quad -f_s \tau f_o \tag{15c}$$

$$s(\theta_l, \varphi_l) = f_s(\rho f_1 + \tau f_2) \quad \text{or} \quad -f_s(\tau f_1 + \rho f_2) \tag{15d}$$

$$s'(\theta_l, \varphi_l) = f_s(\tau f_1 + \rho f_2) \quad \text{or} \quad -f_s(\rho f_1 + \tau f_2) \tag{15e}$$

$$v(\theta_l, \varphi_l) = f_o(\rho f_1 + \tau f_2) \quad \text{or} \quad -f_o(\tau f_1 + \rho f_2) \tag{15f}$$

$$v'(\theta_l, \varphi_l) = f_o(\tau f_1 + \rho f_2) \quad \text{or} \quad -f_o(\rho f_1 + \tau f_2) \tag{15g}$$

$$\sigma(\theta_l, \varphi_l) = f_1(\rho f_1 + \tau f_2) + f_2(\tau f_1 + \rho f_2) \tag{15h}$$

$$\sigma'(\theta_l, \varphi_l) = f_1(\tau f_1 + \rho f_2) + f_2(\rho f_1 + \tau f_2) \tag{15i}$$

$$a(\theta_l, \varphi_l) = 1 - \sigma'(\theta_l, \varphi_l) \tag{15j}$$

where ρ and τ are the leaf reflectance and transmittance, respectively. Negative values of f_s and f_o are used when the lower side of the leaf is illuminated and observed, respectively. The negative values of $f_s f_o$ correspond to the cases that illumination and observation are on opposite sides of the leaf [11]. f_s, f_o, f_1, and f_2 are given by

$$f_s = (s \cdot l) / (s \cdot n) \tag{16a}$$

$$f_o = (o \cdot l) / (o \cdot n) \tag{16b}$$

$$f_1 = (1 + \cos\theta_l) / 2 \tag{16c}$$

$$f_2 = (1 - \cos\theta_l) / 2 \tag{16d}$$

where the vectors l and n are the upward normals to the leaf and the canopy layer, respectively; s and o are the solar and the sensor directions [8], [11]; θ_s and φ_s are the zenith and azimuth angles of the sun, respectively; and θ_o and φ_o are the view zenith and azimuth angle, respectively

$$l = (\sin\theta_l \cos\varphi_l; \ \sin\theta_l \sin\varphi_l; \ \cos\theta_l) \tag{17a}$$

$$n = (0; \ 0; \ 1) \tag{17b}$$

$$s = (\sin\theta_s \cos\varphi_s; \ \sin\theta_s \sin\varphi_s; \ \cos\theta_s) \tag{17c}$$

$$o = (\sin\theta_o \cos\varphi_o; \ \sin\theta_o \sin\varphi_o; \ \cos\theta_o). \tag{17d}$$

For the 4SAIL model over flat surfaces, the leaves are assumed to be uniformly distributed for all azimuths, and the nine coefficients for each particular orientation in (15) are integrated over the azimuth angle φ_l. They are then weighted with the LIDF to obtain the SAIL coefficients for the whole layer [in (13)]

$$c = \int_0^{\pi/2} c(\theta_l) f(\theta_l) d\theta_l \tag{18}$$

where c represents one of the coefficients in (13), $c(\theta_l)$ is the result of integrating the coefficient in (15) over φ_l, which can be found in [11], and $f(\theta_l)$ is the LIDF.

The solution of (13) can be expressed by a set of equations [9], [14]

$$E_s(-1) = \tau_{ss} E_s(0) \tag{19a}$$

$$E^-(-1) = \tau_{sd} E_s(0) + \tau_{dd} E^-(0) + \rho_{dd} E^+(-1) \\ + \gamma_d H_v \tag{19b}$$

$$E^+(0) = \rho_{sd} E_s(0) + \rho_{dd} E^-(0) + \tau_{dd} E^+(-1) \\ + \gamma_d H_v \tag{19c}$$

$$E_o(0) = \rho_{so} E_s(0) + \rho_{do} E^-(0) + \tau_{do} E^+(-1) \\ + \tau_{oo} E_o(-1) + \gamma_o H_v \tag{19d}$$

where ρ and τ represent the reflectances and transmittances of the isolated canopy layer, respectively. Table II gives the physical meaning of the quantities (retaining terminology in [14]), and γ_o and γ_d can be identified as the directional and hemispherical emissivity of the isolated canopy layer, respectively [14]

$$\gamma_o = 1 - \rho_{do} - \tau_{do} - \tau_{oo} \tag{20a}$$

$$\gamma_d = 1 - \rho_{dd} - \tau_{dd}. \tag{20b}$$

If the reflection properties of the soil beneath the canopy layer are expressed by the reflectance terms r_{so}, r_{sd}, r_{do}, and r_{dd} (see Table II for the physical explanations), and the temperature of the soil is T_s, then two equations are added to (19) as the bottom boundary conditions

$$E^+(-1) = r_{sd} E_s(-1) + r_{dd} E^-(-1) + \varepsilon_s^d H_s \tag{21a}$$

$$E_o(-1) = r_{so} E_s(-1) + r_{do} E^-(-1) + \varepsilon_s^o H_s \tag{21b}$$

where H_s is the hemispherical flux calculated for blackbody soil at temperature T_s, and as in (14), $H_s = \pi B(T_s)$. ε_s^o and ε_s^d are the directional and hemispherical emissivities of the soil

$$\varepsilon_s^o = 1 - r_{do} \tag{22a}$$

$$\varepsilon_s^d = 1 - r_{dd}. \tag{22b}$$

By solving (19) and (21), the flux-equivalent radiance in the view direction is given by

$$E_o(0) = r_{so}^* E_s(0) + r_{do}^* E^-(0) + \varepsilon_v^* H_v + \varepsilon_s^* H_s \tag{23}$$

where

$$r_{so}^* = \rho_{so} + \tau_{ssoo} r_{so} \\ + \frac{\tau_{do}(\tau_{ss} r_{sd} + \tau_{sd} r_{dd}) + \tau_{oo} r_{do}(\tau_{sd} + \tau_{ss} r_{sd} \rho_{dd})}{1 - r_{dd} \rho_{dd}} \tag{24a}$$

$$r_{do}^* = \rho_{do} + \frac{(\tau_{do} r_{dd} + \tau_{oo} r_{do}) \tau_{dd}}{1 - r_{dd} \rho_{dd}} \tag{24b}$$

$$\varepsilon_v^* = \rho_{do} + \frac{(\tau_{do} r_{dd} + \tau_{oo} r_{do}) \tau_{dd}}{1 - r_{dd} \rho_{dd}} \tag{24c}$$

$$\varepsilon_s^* = \tau_{oo} \varepsilon_s^o + \frac{(\tau_{do} + \tau_{oo} r_{do} \rho_{dd})}{1 - r_{dd} \rho_{dd}} \varepsilon_s^d. \tag{24d}$$

The above modeling assumes an isothermal canopy layer and an isothermal soil. Verhoef *et al.* [14] also proposed

r_{so}, r_{so}^*	Bi-directional reflectance factor of soil and ensemble system
r_{sd}, r_{sd}^*	Directional-hemispherical reflectance of soil and ensemble system
r_{do}, r_{do}^*	Hemispherical-directional reflectance factor of soil and ensemble system
r_{dd}, r_{dd}^*	Bi-hemispherical reflectance of soil and ensemble system
ρ_{so}	Bi-directional reflectance of the isolated canopy
ρ_{sd}	Directional-hemispherical reflectance of the isolated canopy
ρ_{do}	Hemispherical-directional reflectance of the isolated canopy
ρ_{dd}	Bi-hemispherical reflectance of the isolated canopy
τ_{ss}, τ_{oo}	Direct transmittance of the isolated canopy in incident and observation direction
τ_{sd}	Directional-hemispherical transmittance of the isolated canopy in incident direction
τ_{do}	Hemispherical-directional transmittance of the isolated canopy in observation direction
τ_{dd}	Bi-hemispherical transmittance of the isolated canopy
τ_{ssoo}	Joint two-way directional transmittance of the isolated canopy

a model that considers hot/cold leaves and hot/cold soil, in which (19) and (21) are updated to

$$E_s(-1) = \tau_{ss} E_s(0) \tag{25a}$$

$$E^-(-1) = \tau_{sd} E_s(0) + \tau_{dd} E^-(0) + \rho_{dd} E^+(-1)$$
$$+ \gamma_d H_v + \gamma'_{sd} \varepsilon_v (H_h - H_c) \tag{25b}$$

$$E^+(0) = \rho_{sd} E_s(0) + \rho_{dd} E^-(0) + \tau_{dd} E^+(-1)$$
$$+ \gamma_d H_v + \gamma_{sd} \varepsilon_v (H_h - H_c) \tag{25c}$$

$$E_o(0) = \rho_{so} E_s(0) + \rho_{do} E^-(0) + \tau_{do} E^+(-1)$$
$$+ \tau_{oo} E_o(-1) + \gamma_o H_c + \gamma_{so} \varepsilon_v (H_h - H_c) \tag{25d}$$

$$E^+(-1) = r_{sd} E_s(-1) + r_{dd} E^-(-1) + \varepsilon_s^d H_d$$
$$+ \varepsilon_s^d \tau_{ss} (H_s - H_d) \tag{25e}$$

$$E_o(-1) = r_{so} E_s(-1) + r_{do} E^-(-1) + \varepsilon_s^o H_d$$
$$+ \varepsilon_s^o \tau_{ss} (H_s - H_d) \tag{25f}$$

where H_h, H_c, H_s, and H_d are the hemispherical thermal fluxes associated with the blackbody hot leaves, cold leaves, hot soil, and cold soil, respectively. The three new coefficients $\gamma_{sd}, \gamma'_{sd}$, and γ_{so} are output by 4SAIL, and they take effect only when a temperature difference exists [14]. Similarly, by solving (25), the flux-equivalent radiance in the view direction is given by

$$E_o(0) = r_{so}^* E_s(0) + r_{do}^* E^-(0) + \varepsilon_v^* H_c + \varepsilon_s^* H_d$$
$$+ \varepsilon_v^{**} (H_h - H_c) + \varepsilon_s^{**} (H_s - H_d) \tag{26}$$

where

$$\varepsilon_v^{**} = \left[\gamma_{so} + \frac{(\tau_{do} r_{dd} + \tau_{oo} r_{do})}{1 - r_{dd} \rho_{dd}} \gamma'_{sd} \right] \varepsilon_v \tag{27a}$$

$$\varepsilon_s^{**} = \left[\tau_{ssoo} \varepsilon_s^o + \frac{\tau_{ss} (\tau_{do} + \tau_{oo} r_{do} \rho_{dd})}{1 - r_{dd} \rho_{dd}} \varepsilon_s^d \right]. \tag{27b}$$

Except for the $E_o(0)$, all other fluxes can be obtained. The reflection and emission properties of the ensemble system (soil + canopy) are also inferred [68].

REFERENCES

[1] S. Liang, D. Wang, T. He, and Y. Yu, "Remote sensing of Earth's energy budget: Synthesis and review," *Int. J. Digit. Earth*, vol. 12, no. 7, pp. 737–780, Mar. 2019.

[2] P. J. Sellers *et al.*, "Remote sensing of the land surface for studies of global change: Models—Algorithms—Experiments," *Remote Sens. Environ.*, vol. 51, no. 1, pp. 3–26, Jan. 1995.

[3] M. Jin and S. Liang, "An improved land surface emissivity parameter for land surface models using global remote sensing observations," *J. Climate*, vol. 19, no. 12, pp. 2867–2881, Jun. 2006.

[4] G. L. Stephens, D. O'Brien, P. J. Webster, P. Pilewski, S. Kato, and J.-L. Li, "The albedo of Earth," *Rev. Geophys.*, vol. 53, no. 1, pp. 141–163, Mar. 2015.

[5] G. Duveiller, J. Hooker, and A. Cescatti, "The mark of vegetation change on Earth's surface energy balance," *Nature Commun.*, vol. 9, no. 1, pp. 1–12, Feb. 2018.

[6] A. Kuusk, "Canopy radiative transfer modeling," in *Comprehensive Remote Sensing*, vol. 3, S. Liang, Ed. Oxford, U.K.: Elsevier, 2018, pp. 9–22.

[7] B. Cao *et al.*, "A review of Earth surface thermal radiation directionality observing and modeling: Historical development, current status and perspectives," *Remote Sens. Environ.*, vol. 232, Oct. 2019, Art. no. 111304.

[8] W. Verhoef, "Light scattering by leaf layers with application to canopy reflectance modeling: The SAIL model," *Remote Sens. Environ.*, vol. 16, no. 2, pp. 125–141, Oct. 1984.

[9] W. Verhoef, "Earth observation modeling based on layer scattering matrices," *Remote Sens. Environ.*, vol. 17, no. 2, pp. 165–178, Apr. 1985.

[10] G. Suits, "The calculation of the directional reflectance of a vegetative canopy," *Remote Sens. Environ.*, vol. 2, pp. 117–125, Jan. 1971.

[11] W. Verhoef, "Theory of radiative transfer models applied in optical remote sensing of vegetation canopies," Ph.D. dissertation, Dept. Nat. Aerosp. Lab. NLR, Wageningen Agricult. Univ., Wageningen, The Netherlands, 1998.

[12] A. Kuusk, "The hot spot effect in plant canopy reflectance," in *Photon-Vegetation Interactions: Applications in Optical Remote Sensing and Plant Ecology*, R. Myneni and J. Ross, Eds. Berlin, Germany: Springer-Verlag, 1991, pp. 139–159.

[13] S. Jacquemoud *et al.*, "PROSPECT+SAIL models: A review of use for vegetation characterization," *Remote Sens. Environ.*, vol. 113, no. 1, pp. S56–S66, Sep. 2009.

[14] W. Verhoef, L. Jia, Q. Xiao, and Z. Su, "Unified optical-thermal four-stream radiative transfer theory for homogeneous vegetation canopies," *IEEE Trans. Geosci. Remote Sens.*, vol. 45, no. 6, pp. 1808–1822, Jun. 2007.

[15] A. Mousivand, W. Verhoef, M. Menenti, and B. Gorte, "Modeling top of atmosphere radiance over heterogeneous non-lambertian rugged terrain," *Remote Sens.*, vol. 7, no. 6, pp. 8019–8044, Jun. 2015.

[16] A. E. Lipton, "Effects of slope and aspect variations on satellite surface temperature retrievals and mesoscale analysis in mountainous terrain," *J. Appl. Meteorol.*, vol. 31, no. 3, pp. 255–264, Mar. 1992.

[17] A. Lipton, "Satellite-view biases in retrieved surface temperatures in mountain areas," *Remote Sens. Environ.*, vol. 60, no. 1, pp. 92–100, Apr. 1997.

[18] F. Gemmell, "An investigation of terrain effects on the inversion of a forest reflectance model," *Remote Sens. Environ.*, vol. 65, no. 2, pp. 155–169, Aug. 1998.

[19] K. Wang, X. Zhou, J. Liu, and M. Sparrow, "Estimating surface solar radiation over complex terrain using moderate-resolution satellite sensor data," *Int. J. Remote Sens.*, vol. 26, no. 1, pp. 47–58, Jan. 2005.

[20] Y. Chen, A. Hall, and K. N. Liou, "Application of three-dimensional solar radiative transfer to mountains," *J. Geophys. Res.*, vol. 111, no. D21, Nov. 2006, Art. no. D21111.

[21] A. Gonsamo and P. Pellikka, "Methodology comparison for slope correction in canopy leaf area index estimation using hemispherical photography," *Forest Ecology Manage.*, vol. 256, no. 4, pp. 749–759, Aug. 2008.

[22] E. M. Luisa, B. Frédéric, and W. Marie, "Slope correction for LAI estimation from gap fraction measurements," *Agricult. Forest Meteorol.*, vol. 148, no. 10, pp. 1553–1562, Sep. 2008.

[23] W.-L. Lee, K. N. Liou, and A. Hall, "Parameterization of solar fluxes over mountain surfaces for application to climate models," *J. Geophys. Res.*, vol. 116, no. D1, Jan. 2011, Art. no. D01101.

[24] B. Gao, L. Jia, and M. Menenti, "An improved method for retrieving land surface albedo over rugged terrain," *IEEE Geosci. Remote Sens. Lett.*, vol. 11, no. 2, pp. 554–558, Feb. 2014.

[25] A. Gonsamo and J. M. Chen, "Improved LAI algorithm implementation to MODIS data by incorporating background, topography, and foliage clumping information," *IEEE Trans. Geosci. Remote Sens.*, vol. 52, no. 2, pp. 1076–1088, Feb. 2014.

[26] Y. Liu, T. Hiyama, and Y. Yamaguchi, "Scaling of land surface temperature using satellite data: A case examination on ASTER and MODIS products over a heterogeneous terrain area," *Remote Sens. Environ.*, vol. 105, no. 2, pp. 115–128, Nov. 2006.

[27] G. Yan, T. Wang, Z. Jiao, X. Mu, J. Zhao, and L. Chen, "Topographic radiation modeling and spatial scaling of clear-sky land surface long-wave radiation over rugged terrain," *Remote Sens. Environ.*, vol. 172, pp. 15–27, Jan. 2016.

[28] P. Zhao, W. Fan, Y. Liu, X. Mu, X. Xu, and J. Peng, "Study of the remote sensing model of FAPAR over rugged terrains," *Remote Sens.*, vol. 8, no. 4, p. 309, Apr. 2016.

[29] H. Jin, A. Li, W. Xu, Z. Xiao, J. Jiang, and H. Xue, "Evaluation of topographic effects on multiscale leaf area index estimation using remotely sensed observations from multiple sensors," *ISPRS J. Photogramm. Remote Sens.*, vol. 154, pp. 176–188, Aug. 2019.

[30] Y. Wu, N. Wang, Z. Li, A. Chen, Z. Guo, and Y. Qie, "The effect of thermal radiation from surrounding terrain on glacier surface temperatures retrieved from remote sensing data: A case study from Qiyi Glacier, China," *Remote Sens. Environ.*, vol. 231, Sep. 2019, Art. no. 111267.

[31] G. Yan, Z.-H. Jiao, T. Wang, and X. Mu, "Modeling surface longwave radiation over high-relief terrain," *Remote Sens. Environ.*, vol. 237, Feb. 2020, Art. no. 111556.

[32] W. Yu *et al.*, "A simulation-based analysis of topographic effects on LAI inversion over sloped terrain," *IEEE J. Sel. Topics Appl. Earth Observ. Remote Sens.*, vol. 13, pp. 794–806, Feb. 2020. [Online]. Available: https://ieeexplore.ieee.org/abstract/document/8995536

[33] C. B. Schaaf, X. Li, and A. H. Strahler, "Topographic effects on bidirectional and hemispherical reflectances calculated with a geometric-optical canopy model," *IEEE Trans. Geosci. Remote Sens.*, vol. 32, no. 6, pp. 1186–1193, Nov. 1994.

[34] W. Fan, J. M. Chen, W. Ju, and G. Zhu, "GOST: A geometric-optical model for sloping terrains," *IEEE Trans. Geosci. Remote Sens.*, vol. 52, no. 9, pp. 5469–5482, Sep. 2014.

[35] B. Combal, H. Isaka, and C. Trotter, "Extending a turbid medium BRDF model to allow sloping terrain with a vertical plant stand," *IEEE Trans. Geosci. Remote Sens.*, vol. 38, no. 2, pp. 798–810, Mar. 2000.

[36] G. Yin, A. Li, W. Zhao, H. Jin, J. Bian, and S. Wu, "Modeling canopy reflectance over sloping terrain based on path length correction," *IEEE Trans. Geosci. Remote Sens.*, vol. 55, no. 8, pp. 4597–4609, Aug. 2017.

[37] W. Fan, J. M. Chen, W. Ju, and N. Nesbitt, "Hybrid geometric optical–radiative transfer model suitable for forests on slopes," *IEEE Trans. Geosci. Remote Sens.*, vol. 52, no. 9, pp. 5579–5586, Sep. 2014.

[38] W. Fan, J. Li, and Q. Liu, "GOST2: The improvement of the canopy reflectance model GOST in separating the sunlit and shaded leaves," *IEEE J. Sel. Topics Appl. Earth Observ. Remote Sens.*, vol. 8, no. 4, pp. 1423–1431, Apr. 2015.

[39] J. Geng *et al.*, "GOFP: A geometric-optical model for forest plantations," *IEEE Trans. Geosci. Remote Sens.*, vol. 55, no. 9, pp. 5230–5241, Sep. 2017.

[40] S. Wu *et al.*, "Modeling discrete forest anisotropic reflectance over a sloped surface with an extended GOMS and SAIL model," *IEEE Trans. Geosci. Remote Sens.*, vol. 57, no. 2, pp. 944–957, Feb. 2019.

[41] D. Gratton, P. Howarth, and D. Marceau, "Using Landsat-5 thematic mapper and digital elevation data to determine the net radiation field of a mountain glacier," *Remote Sens. Environ.*, vol. 43, no. 3, pp. 315–331, Mar. 1993.

[42] C. R. Duguay, "An approach to the estimation of surface net radiation in mountain areas using remote sensing and digital terrain data," *Theor. Appl. Climatol.*, vol. 52, nos. 1–2, pp. 55–68, 1995.

[43] C. Plüss and A. Ohmura, "Longwave radiation on snow-covered mountainous surfaces," *J. Appl. Meteorol.*, vol. 36, no. 6, pp. 818–824, Jun. 1997.

[44] M. D. Müller and D. Scherer, "A grid- and subgrid-scale radiation parameterization of topographic effects for mesoscale weather forecast models," *Monthly Weather Rev.*, vol. 133, no. 6, pp. 1431–1442, Jun. 2005.

[45] J. E. Sicart, J. W. Pomeroy, R. L. H. Essery, and D. Bewley, "Incoming longwave radiation to melting snow: Observations, sensitivity and estimation in northern environments," *Hydrological Processes*, vol. 20, no. 17, pp. 3697–3708, 2006.

[46] Z.-H. Jiao, G. Yan, T. Wang, X. Mu, and J. Zhao, "Modeling of land surface thermal anisotropy based on directional and equivalent brightness temperatures over complex terrain," *IEEE J. Sel. Topics Appl. Earth Observ. Remote Sens.*, vol. 12, no. 2, pp. 410–423, Feb. 2019.

[47] P. M. Teillet, B. Guindon, and D. G. Goodenough, "On the slope-aspect correction of multispectral scanner data," *Can. J. Remote Sens.*, vol. 8, no. 2, pp. 84–106, Dec. 1982.

[48] H. Huang, W. Qin, and Q. Liu, "RAPID: A radiosity applicable to porous individual objects for directional reflectance over complex vegetated scenes," *Remote Sens. Environ.*, vol. 132, pp. 221–237, May 2013.

[49] E. Grau and J.-P. Gastellu-Etchegorry, "Radiative transfer modeling in the Earth–atmosphere system with DART model," *Remote Sens. Environ.*, vol. 139, pp. 149–170, Dec. 2013.

[50] J.-P. Gastellu-Etchegorry *et al.*, "Discrete anisotropic radiative transfer (DART 5) for modeling airborne and satellite spectroradiometer and LIDAR acquisitions of natural and urban landscapes," *Remote Sens.*, vol. 7, no. 2, pp. 1667–1701, Feb. 2015.

[51] J.-P. Gastellu-Etchegorry *et al.*, "DART: Recent advances in remote sensing data modeling with atmosphere, polarization, and chlorophyll fluorescence," *IEEE J. Sel. Topics Appl. Earth Observ. Remote Sens.*, vol. 10, no. 6, pp. 2640–2649, Jun. 2017.

[52] S.-Y. Jin and J. Susaki, "A 3-D topographic-relief-correlated monte carlo radiative transfer simulator for forest bidirectional reflectance estimation," *IEEE Geosci. Remote Sens. Lett.*, vol. 14, no. 6, pp. 964–968, Jun. 2017.

[53] J. Qi *et al.*, "LESS: Large-scale remote sensing data and image simulation framework over heterogeneous 3D scenes," *Remote Sens. Environ.*, vol. 221, pp. 695–706, Feb. 2019.

[54] C. Proy, D. Tanré, and P. Y. Deschamps, "Evaluation of topographic effects in remotely sensed data," *Remote Sens. Environ.*, vol. 30, no. 1, pp. 21–32, Oct. 1989.

[55] P. Sirguey, "Simple correction of multiple reflection effects in rugged terrain," *Int. J. Remote Sens.*, vol. 30, no. 4, pp. 1075–1081, Feb. 2009.

[56] J. Dozier, J. Bruno, and P. Downey, "A faster solution to the horizon problem," *Comput. Geosci.*, vol. 7, no. 2, pp. 145–151, Jan. 1981.

[57] J. Dozier and J. Frew, "Rapid calculation of terrain parameters for radiation modeling from digital elevation data," *IEEE Trans. Geosci. Remote Sens.*, vol. 28, no. 5, pp. 963–969, Sep. 1990.

[58] J. E. Hay, "Calculating solar radiation for inclined surfaces: Practical approaches," *Renew. Energy*, vol. 3, nos. 4–5, pp. 373–380, Jun. 1993.

[59] B. Y. H. Liu and R. C. Jordan, "The interrelationship and characteristic distribution of direct, diffuse and total solar radiation," *Sol. Energy*, vol. 4, no. 3, pp. 1–19, Jul. 1960.

[60] J. Steenbergen, "Computing sky view factors from geo-data using a GIS," M.S. thesis, Lab. Geo-Inf. Sci. Remote Sens., Wageningen Univ., Wageningen, The Netherlands, Jun. 2009.

[61] J. Rakovec and K. Zakšek, "On the proper analytical expression for the sky-view factor and the diffuse irradiation of a slope for an isotropic sky," *Renew. Energy*, vol. 37, no. 1, pp. 440–444, Jan. 2012.

[62] Z.-H. Jiao, H. Ren, X. Mu, J. Zhao, T. Wang, and J. Dong, "Evaluation of four sky view factor algorithms using digital surface and elevation model data," *Earth Space Sci.*, vol. 6, no. 2, pp. 222–237, Feb. 2019.

[63] J. Pisek, O. Sonnentag, A. D. Richardson, and M. Mõttus, "Is the spherical leaf inclination angle distribution a valid assumption for temperate and boreal broadleaf tree species?" *Agricult. Forest Meteorol.*, vol. 169, pp. 186–194, Feb. 2013.

[64] S. Jacquemoud and F. Baret, "PROSPECT: A model of leaf optical properties spectra," *Remote Sens. Environ.*, vol. 34, no. 2, pp. 75–91, Nov. 1990.

[65] J. Wen *et al.*, "Characterizing land surface anisotropic reflectance over rugged terrain: A review of concepts and recent developments," *Remote Sens.*, vol. 10, no. 3, p. 370, Feb. 2018.

[66] D. Hao *et al.*, "Modeling anisotropic reflectance over composite sloping terrain," *IEEE Trans. Geosci. Remote Sens.*, vol. 56, no. 7, pp. 3903–3923, Jul. 2018.

[67] S. Wu *et al.*, "The definition of remotely sensed reflectance quantities suitable for rugged terrain," *Remote Sens. Environ.*, vol. 225, pp. 403–415, May 2019.

[68] W. Verhoef and H. Bach, "Coupled soil-leaf-canopy and atmosphere radiative transfer modeling to simulate hyperspectral multi-angular surface reflectance and TOA radiance data," *Remote Sens. Environ.*, vol. 109, no. 2, pp. 166–182, Jul. 2007.
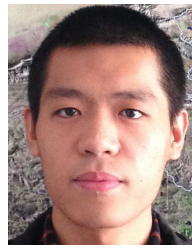
Hanyu Shi (Student Member, IEEE) received the B.S. and M.S. degrees from Beijing Normal University, Beijing, China, in 2014 and 2017, respectively, where he is pursuing the Ph.D. degree.

His research interests include radiative transfer and estimation of surface variables.

Zhiqiang Xiao (Member, IEEE) received the Ph.D. degree in geophysical prospecting and information technology from Central South University, Changsha, China, in 2004.

From 2004 to 2006, he was a Post-Doctoral Research Associate with Beijing Normal University, Beijing, China, where he is a Professor with the Faculty of Geographical Science. His research focuses on retrieval of land biophysical parameters from remotely sensed data, assimilating radiometric observations into dynamic models.